Solution-State Molecular Structure of Apo and Oleate-Liganded Liver Fatty Acid-Binding Protein†

Yan He,‡,§ Xiaomin Yang,‡,§ Hsin Wang,‡ Rima Estephan,‡ Fouad Francis,‡ Sarala Kodukula,|| Judith Storch,*,|| and Ruth E. Stark*,‡,⊥

Department of Chemistry, College of Staten Island, and Graduate Center and Institute for Macromolecular Assemblies, City University of New York, 2800 Victory Boulevard, Staten Island, New York 10314-6600, and Department of Nutritional Sciences, School of Environmental and Biological Sciences, Rutgers University, New Brunswick, New Jersey 08901-8525

Received June 7, 2007; Revised Manuscript Received August 20, 2007

ABSTRACT: Rat liver fatty acid-binding protein (LFABP) is distinctive among intracellular lipid-binding proteins (iLBPs): more than one molecule of long-chain fatty acid and a variety of diverse ligands can be bound within its large cavity, and in vitro lipid transfer to model membranes follows a mechanism that is diffusion-controlled rather than mediated by protein−membrane collisions. Because the apoprotein has proven resistant to crystallization, nuclear magnetic resonance spectroscopy offers a unique route to functionally informative comparisons of molecular structure and dynamics for LFABP in free (apo) and liganded (holo) forms. We report herein the solution-state structures determined for apo-LFABP at pH 6.0 and for holoprotein liganded to two oleates at pH 7.0, as well as the structure of the complex including locations of the ligands. ^{1}H, ^{13}C, and ^{15}N resonance assignments revealed very similar types and locations of secondary structural elements for apo- and holo-LFABP as judged from chemical shift indices. The solution-state tertiary structures of the proteins were derived with the CNS/ARIA computational protocol, using distance and angular restraints based on ^{1}H−^{1}H nuclear Overhauser effects (NOEs), hydrogen-bonding networks, ^{3}J(HNHA) coupling constants, intermolecular NOEs, and residual dipolar (NH) couplings. The holo-LFABP solution-state conformation is in substantial agreement with a previously reported X-ray structure [Thompson, J., Winter, N., Terwey, D., Bratt, J., and Banaszak, L. (1997) The crystal structure of the liver fatty acid-binding protein. A complex with two bound oleates, *J. Biol. Chem. 272*, 7140−7150], including the typical β-barrel capped by a helix−turn−helix portal. In the solution state, the internally bound oleate has the expected U-shaped conformation and is tethered electrostatically, but the extended portal ligand can adopt a range of conformations based on the computationally refined structures, in contrast to the single conformation observed in the crystal structure. The apo-LFABP also has a well-defined β-barrel structural motif typical of other members of the iLBP protein family, but the portal region that is thought to facilitate ligand entry and exit exhibits conformational variability and an unusual "open cap" orientation with respect to the barrel. These structural results allow us to propose a model in which ligand binding to LFABP occurs through conformational fluctuations that adjust the helix−turn−helix motif to open or close the top of the β-barrel, and solvent accessibility to the protein cavity favors diffusion-controlled ligand transport.

Liver fatty acid-binding protein (LFABP)[1] belongs to a family of 14−15 kDa intracellular lipid-binding proteins (iLBPs) that have 126−134 amino acids and the ability to bind long-chain fatty acids (FA) and in some cases other small hydrophobic ligands (*2*−*7*). It is thought that these proteins facilitate intracellular lipid transport in aqueous media as well as lipid uptake and metabolic regulation through interactions with lipids, membranes, and other cellular proteins. LFABP is found abundantly in the small intestine and liver and to a lesser extent in the kidney and colon. The concurrent expression of LFABP with IFABP, ILBP, and CRBP(II) in the small intestine suggests a functional specificity for different family members (*4*, *8*), though in liver tissues LFABP is the only FABP expressed at a high level, where it coexists with cellular retinol-binding

† This work was supported by grants from the National Institutes of Health (DK38389) and the Professional Staff Congress of the City University of New York (CUNY) (69181, 61209, and 80209) and pilot funding from a Rutgers University C. and J. Busch Biomedical Research Grant. The Ph.D. work of R.E. was supported by a Minority Supplement from the National Institutes of Health. Operation of the NMR facility was supported by the College of Staten Island and the CUNY Institute for Macromolecular Assemblies, a Center of Excellence of the Generating Employment through New York State Science program. The 800 MHz NMR spectrometer was supported by NIH Grant P41 GM66354 to the New York Structural Biology Center, a STAR center supported by the New York State Office of Science, Technology, and Academic Research.

* To whom correspondence should be addressed. (R.E.S.) E-mail: stark@sci.ccny.cuny.edu. Phone: (212) 650-8916. Fax: (212) 650-6107. (J.S.) E-mail: storch@aesop.rutgers.edu. Phone: (732) 932-1689. Fax: (732) 932-3769.

‡ City University of New York.

§ These authors contributed equally to this work.

|| Rutgers University.

⊥ Current address: CUNY Institute for Macromolecular Assemblies, Department of Chemistry, The City College of New York, Convent Ave. at 138th St., New York, NY 10031.

[1] Abbreviations: LFABP, liver fatty acid-binding protein from rat; iLBP, intracellular lipid-binding protein; FA, long-chain fatty acid; FABP, fatty acid-binding protein; AFABP, adipocyte fatty acid-binding protein; BFABP, brain fatty acid-binding protein; EFABP, epidermal fatty acid-binding protein; HFABP, heart fatty acid-binding protein; IFABP, intestinal fatty acid-binding protein; MFABP, myelin fatty acid-binding protein; ILBP, ileal lipid-binding protein; CRBP, cellular retinol-binding protein; CRABP, cellular retinoic acid-binding protein; NMR, nuclear magnetic resonance; NOESY, nuclear Overhauser effect spectroscopy; RDC, residual dipolar coupling; rmsd, root mean square deviation; OLA, oleate.

10.1021/bi701092r CCC: $37.00 © 2007 American Chemical Society
Published on Web 10/10/2007

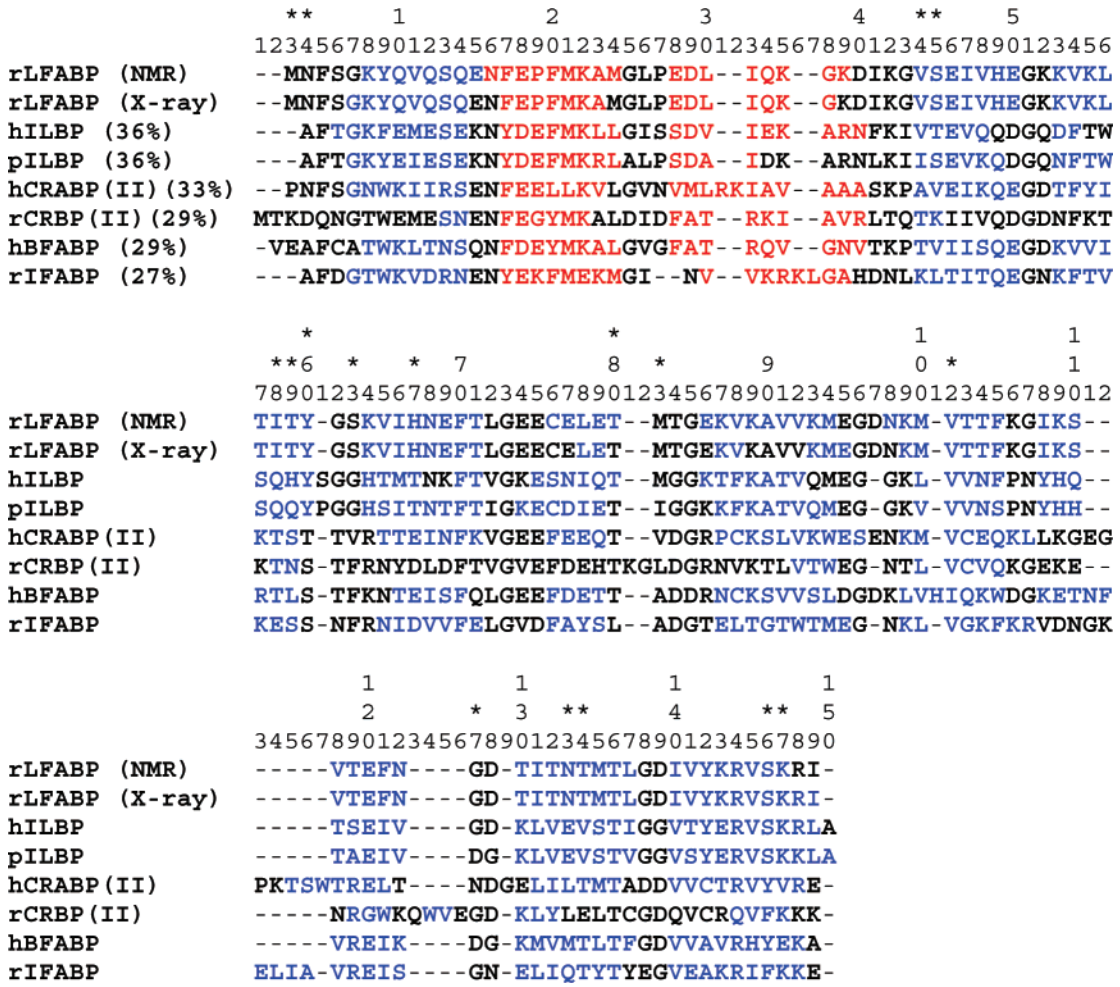

FIGURE 1: Sequence alignment of LFABP with other iLBP protein family members from www.biochem.ucl.ac.uk, showing percentage sequence identities in parentheses. Key: h, human; p, porcine; r, rat; BFABP, brain fatty acid-binding protein; CRABP, cellular retinoic acid-binding protein; CRBP, cellular retinol-binding protein; IFABP, intestinal fatty acid-binding protein; ILBP, ileal lipid-binding protein; LFABP, liver fatty acid-binding protein. The secondary structures adopted by various amino acid residues, deduced from either X-ray or NMR structures, are shown in red (α-helix) and blue (*β*-strand). Residues labeled with an asterisk denote missing amide NH resonances reported previously (*44*) in HSQC NMR of the unliganded rLFABP protein at pH 6.

protein (CRBP(I)). Within the family of iLBPs, LFABP displays the highest sequence identity to ILBP (see Figure 1), possibly accounting for its capacity to bind more bulky, hydrophobic ligands. It has been reported that LFABP binds two fatty acid molecules in vitro (rather than the usual single ligand) (*9*−*12*), and it can also bind bile salts, acyl-CoA esters, bromosulphthalein, lysophospholipids, monoglycerides, and other hydrophobic compounds (*2*, *6*, *13*). Besides these unique binding specificities, LFABP is distinguished from other family members by its diffusion-mediated mechanism of fatty acid transport in vitro (*4*, *14*, *15*), which is shared only with CRBPII, and which contrasts with the protein−membrane collisional process typical of HFABP, AFABP, BFABP, MFABP, IFABP, and CRBP(I) (*16*).

In recent years, the structures and dynamic properties of iLBPs in both apo and holo forms have been studied extensively by X-ray and NMR techniques (*1*, *7*, *17*−*31*). All iLBPs have a common structural motif: a *β*-barrel comprised of 10 antiparallel *β*-strands, forming an interior ligand-binding cavity, and a short helix−turn−helix lid that caps one end of the *β*-barrel. The structural similarity often found between apo and holo forms supports a mechanistic hypothesis in which the helix−turn−helix region and its neighboring turns between *β*-strands form a portal to the protein cavity, allowing ligand entry and exit without significant overall protein structural changes. This hypothesis is in accord with the observation that most iLBP structures, including IFABP (*18*), ILBP (*29*), EFABP (*23*, *27*), MFABP (*32*), and HFABP (*25*), exhibit conformational variability primarily in the portal region. In a few cases such as CRBP-(II) (*19*, *33*), CRABP(I) (*34*), and CRABP(II) (*35*, *36*), however, the helix−turn−helix and neighboring turns are thought to exist in an open apo state but undergo conformational changes to a closed, liganded state. Such an open−close event is supported by limited proteolysis studies on LFABP, CRABP(I), CRBP(I), and CRBP(II) (*37*, *38*), which indicate that the apoproteins are more susceptible to degradation than the corresponding holo analogues. Protein flexibility has been proposed to facilitate accommodation of bulky ligands such as bile salts by ILBP and LFABP (*39*).

Regardless of whether apo-FABPs form a portal or exist in the open state, the importance of the helix−turn−helix region to the biological functions of fatty acid binding and transport is clear. Fatty acid transport studies show that HFABP, AFABP, and IFABP, which transfer ligand to membranes by a collision-mediated mechanism, have helical

regions that interact directly with the membrane (*4*, *40*). A helixless variant of IFABP maintains a conformation nearly identical to the β-sheets of the wild-type protein (*41*) but is less resistant to denaturation. It also adopts a diffusion-controlled mechanism of fatty acid transfer (*41*−*43*), suggesting that the helix−turn−helix domain is critical for IFABP−membrane interactions involved in fatty acid transport.

The crystal structure of LFABP with oleate (holo-LFABP) (*1*) shows two FAs bound within the central cavity: one in a U-shaped conformation with the carboxylate group in proximity to the R122, S124, and S39 side chains and another in an extended conformation for which the carboxylate moiety interacts with K31 and S56 side chains located near the protein surface in the portal region. LFABP has the largest cavity size in the iLBP family, attributable, in large part, to the replacement of bulky side chains by more compact groups (*11*): e.g., L38, K92, and R106 in IFABP compared with S39, T94, and F104 in LFABP. Given the above-mentioned differences in ligand specificity and stoichiometry for LFABP relative to FABPs that bind only a single molecule of fatty acid, the observation of a common β-barrel structure for all FABP family members suggests that the key to the binding affinity and ligand specificity of LFABP may lie in its cavity and portal regions, making it imperative to characterize those regions structurally. Further, surface properties of the iLBPs are likely to dictate specific interactions with protein and/or membrane partners and may differ for the ligand-free and ligand-bound states (*15*). Because there is no crystal structure available for apo-LFABP, NMR measurements in the solution state offer a unique tool for the comparison of holo- and apo-LFABP conformations.

Our prior chemical shift assignments for apo-LFABP in aqueous solution provided chemical shift indices indicative of secondary structural elements that correspond closely to crystalline holo-LFABP (*1*, *44*), but the three-dimensional arrangement of the 2 helices and 10 β-strands in the unliganded protein remained elusive (*45*). Also, although our solution-state NMR titrations of the protein with uniformly ^{13}C-labeled oleate confirmed that two molecules of the fatty acid reside in the LFABP cavity (*46*), they did not address the issue of where the ligands are situated within the protein interior. Here, we report multidimensional NMR results including intra- and intermolecular nuclear Overhauser effects as well as residual dipolar couplings, allowing for detailed structural comparisons of holo-LFABP and apo-LFABP that may inform hypotheses regarding the mechanisms of cellular lipid binding and transport for this unique member of the iLBP protein family.

MATERIALS AND METHODS

Expression and Purification of LFABP. The expression and purification of recombinant LFABP from *Escherichia coli* were conducted as described previously (*44*) or using a modified expression method to increase the yield of isotopically labeled protein (*47*). Rat liver FABP cDNA was subcloned into the pET-11a expression vector using two restriction enzyme sites, *Nde*I and *Bam*H1, and the expression vector along with the insert was transformed into *E. coli* host strain BL21(DE3) or BL21(DE3)pLys. In the modified procedure, *E. coli* cells were first grown rapidly in unlabeled rich medium to high cell densities with $OD_{600\ nm} \approx 0.6$, then exchanged into M9 minimal medium consisting of $^{15}NH_4Cl$ and [U-$^{13}C_6$]glucose (Isotec, Miamisburg, OH) at higher cell densities that were optimized to achieve maximal protein expression, and finally allowed to recover for 1 h. Protein expression was induced by adding 1.0 mM IPTG to the growing cell culture at 37 °C for 3 h. The cells were harvested and resuspended in pH 8.3 Tris buffer for subsequent LFABP purification and delipidation (*14*). Typical yields of pure protein were 30 mg/L of culture. The purity of the LFABP protein was assessed by SDS−PAGE gel electrophoresis, which displayed a single band corresponding to a size of 14 kDa.

Preparation of NMR Samples. For apo-LFABP samples, the uniformly ^{15}N- or ^{15}N/^{13}C-enriched purified proteins were concentrated by Centriprep-10 or Centricon-10 ultrafiltration (Millipore, Bedford, MA), exchanged with an appropriate buffer, and concentrated to 0.5−1.3 mM in pH 6.0 phosphate buffer containing 50 mM NaP_i, 5 μM EDTA, 5% D_2O, and 0.02% sodium azide. For preparation of holo-LFABP with bound oleic acid, [U-^{15}N]- or [U-^{15}N/^{13}C]LFABP samples were transferred into $(NH_4)_2CO_3$ buffer by passing them through a PD-10 gel filtration column (Pharmacia, Piscataway, NJ) and then incubated overnight at 4 °C with 5 mM sodium oleate at pH 9.6 to achieve a protein-to-oleate ratio of 1:3. The mixture was subjected to Centricon-10 ultrafiltration (Millipore) with a pH 7.0 phosphate buffer containing 50 mM NaP_i, 100 mM NaCl, and 5 μM EDTA to reduce the volume and achieve a final concentration of 0.7−1.0 mM protein. For H/D exchange studies and 3D/4D ^{13}C-edited nuclear Overhauser enhancement spectroscopy (NOESY) experiments, the protein was lyophilized and then dissolved in 99% D_2O buffer. For NMR studies of intermolecular protein−ligand interactions, holo-LFABP samples were made from U-^{15}N-labeled protein with [U-^{13}C]oleic acid (Isotec) as well as U-^{15}N/^{13}C-labeled protein with natural abundance oleic acid. The sample used for residual dipolar coupling measurements was prepared by exchanging and concentrating the ^{15}N-labeled apo-LFABP into pH 7.0 phosphate buffer and then mixing with 15% (w/w) *n*-dodecylpenta(ethylene glycol)/hexanol ($C_{12}E_5$) alignment medium (Sigma-Aldrich, St. Louis, MO) (*48*) to achieve final concentrations of about 0.3 mM and 5% for protein and $C_{12}E_5$, respectively. Protein concentrations were assayed as described previously (*46*).

NMR Experiments and Analysis. The majority of the NMR experiments were performed using a four-channel Varian ^{UNITY}INOVA 600 MHz spectrometer operating at 30 °C and chemical shift referencing according to the guidelines of Wishart et al. (*49*). As described previously (*44*), sequential assignments of ^{1}H, ^{15}N, and ^{13}C nuclei were made by standard through-bond correlation procedures using data from 2D ^{15}N HSQC, 3D CBCA(CO)NH, HNCACB, HNCO, CBCACOHA, TOCSY-HSQC(^{15}N), H(CCO)NH-TOCSY, C(CO)NH-TOCSY, and HCCH-TOCSY (*50*). Additional experiments, including HBCBCDHD and HBCBCDCEHE (*51*), CGCBHB, CGCDHD, and CGCDCEHE (*52*), CT-HMQC-COSY (*53*), and hisHCN (*54*), were also carried out to make aromatic side chain assignments for Phe, Tyr, and His residues. All multidimensional NMR data were processed with the NMRPipe program (*55*) and analyzed using NMR-

View software (*56*). The resonance assignments were submitted to the BioMagResBank under accession numbers 15429, 15433, and 15434 for apo, holo, and complex forms, respectively.

Distance restraints for the structure calculations were derived from several multidimensional NOESY experiments that identify proton pairs within 5 Å of one another: ^{15}N-edited 3D NOESY (*57*), ^{13}C-edited 3D and 4D NOESY, and ^{15}N/^{13}C-edited 4D NOESY (*50*). As noted above, intermolecular NOESY experiments were conducted on samples of [U-^{15}N/^{13}C]LFABP complexed with unlabeled oleate and [U-^{15}N]LFABP with [U-^{13}C]oleate. The 3D ^{13}C-filtered,^{13}C-edited intermolecular NOE measurements (*58*) were conducted at 600 MHz (as described above) and also at 800 MHz on a Bruker AVANCE II spectrometer located at the New York Structural Biology Center. Mixing times of 150 ms were used in all NOESY experiments.

Cross-peaks in the NOESY spectra were picked automatically by the NMRView program and verified carefully by hand; the program also provided lists of possible assignments based on chemical shift trends and/or preliminary three-dimensional structures. As expected, ^{13}C-edited and ^{15}N-edited 3D NOESY data yielded unambiguous assignments of numerous intraresidue and sequential NOEs but just a small number of medium- and long-range NOEs; ^{13}C/^{13}C-edited 4D NOESY and ^{15}N/^{13}C-edited 4D NOESY provided medium- and long-range NOE connectivities that were crucial at the beginning of the analysis when no preliminary structure was available. Approximately 60% of the NOEs were assigned unambiguously at this stage, and the remainder were entered into the ARIA program as ambiguous NOEs (see the procedure below).

Three-bond *J* coupling constants ($^3J_{H^N H^\alpha}$) derived from 3D HNHA experiments (*59*) on both apo- and holo-LFABP were converted into backbone torsion angle (ϕ) restraints using ARIA/CNS and coefficients of 6.98, −1.38, and 1.72 in the Karplus equation (*50*). Additional dihedral angle restraints were derived from predictions of the TALOS program (*60*), which matches the amino acid sequence and measured chemical shifts to a structural database.

The hydrogen bonds that held together the β-sheets were deduced from identification of interstrand NOE connectivities and amide protons that were protected from the aqueous solvent in hydrogen−deuterium exchange experiments. In total, 34 and 45 hydrogen-bonding restraints were defined for holo-LFABP and apo-LFABP, respectively. For apo-LFABP, four additional hydrogen-bonding restraints within the two helices were deduced from the observed NOE patterns of α-protons, NH protons, and β-protons [$d_{\alpha N}(i, i + 3)$, $d_{\alpha N}(i, i + 4)$, and $d_{\alpha\beta}(i, i + 3)$], as well as H/D exchange data. In-phase/antiphase ^{15}N HSQC experiments (*61*) were carried out to measure residual N−H dipolar couplings. In the case of apo-LFABP, 57 residual dipolar coupling constraints were also incorporated into the structure calculation.

Structure Calculations from NMR-Based Restraints. NMR-based structure calculations were performed using the programs CNS (version 1.1) (*62*) and ARIA (version 2.0 with water refinement for the apo- and holoproteins, version 1.2_dani for the protein−ligand complex) (*63, 64*). Initial random coil conformations were used for all protein and ligand molecules. The first structure calculations were performed by CNS using manually assigned NOE-derived distance restraints. Additional NOE assignments, especially medium- and long-range proximities, were then deduced on the basis of the lowest energy preliminary structures and added to the list of unambiguous NOEs. The converged structures from CNS were then used for iterative automated assignments of the NOE spectra by ARIA, which integrates with CNS for structure refinement. ARIA-assisted assignments were checked manually and confirmed. The CNS/ARIA procedure involved simulated annealing followed by 200 steps of restrained Powell energy minimization. For apo-LFABP, the 10 structures with lowest energy were selected for deposition in the Protein Data Bank (PDB) (ID code 2ju3). For holo-LFABP complexed to two oleate ligands, the calculations were begun with a random coil protein conformation and 2614 intramolecular NOE restraints; the resulting deposition had ID code 2ju7. For the oleate-LFABP complex, calculations were conducted analogously by including two energy-optimized ligand structures and an additional 67 intermolecular NOE restraints; the 10 structures that balanced the lowest energy with a consistent orientation of the ligands were also deposited in the PDB (ID code 2ju8). Structural results were visualized with MOLMOL 2K.2 (ETH, Zurich, Switzerland) and Discovery Studio (DS) ViewerPro 6.0 (Accelrys Software, San Diego, CA).

RESULTS

Resonance Assignments and Secondary Structural Elements for Holo-LFABP. Resonance assignments for holo-LFABP liganded to two molecules of oleate (OLA) were made following the protocol reported previously for apo-LFABP (*44*) and augmented by experiments tailored for the aromatic side chain nuclei (*51*−*54*), as described above. Unlike apo-LFABP, for which 15 amide NH resonances were missing from ^{1}H−^{15}N HSQC spectra of previous samples (Figure 1) (*44*) and G45, T53, S56, M74, G106, and D107 were absent at pH 7, in holo-LFABP those residues were observable, suggesting that oleate binding stabilizes the LFABP structure and diminishes the conformational exchange broadening of polypeptide backbone signals. Assignment tables for ^{1}H, ^{13}C, and ^{15}N nuclei of both forms of LFABP are available as Supporting Information and have been deposited in the BioMagResBank.

The sensitivity of H_α, C_α, CO, and C_β chemical shifts to α-helix and β-strand chemical environments is well established and codified by use of consensus ^{1}H/^{13}C chemical shift indices (CSIs) (*65*) to deduce the secondary structure. Thus, it was possible to make provisional designations of secondary structural elements for holo-LFABP (Figure 2), independently of further analyses using NOEs or other geometric restraints. From the CSI values shown for H_α, C_α, CO, and C_β resonances in Figure 2A−D, the derived consensus values of −1, 0, and 1 (Figure 2E) served to locate α-helix, coil or loop, and β-strand structures, respectively (*49*). For comparison, the consensus CSI profile for apo-LFABP (*44*) is displayed as Figure 2F. Except for minor variations at the boundaries between elements that are indicated by the apoprotein residue numbers listed in italics, it was possible to identify 10 β-strands spanning the sequences K6−E13, V38−E44, K46−Y54, K57−T64, C69−T73, E77−M85/*E86*, N89−F95, I98−N105, T108−L115, and I118−K125

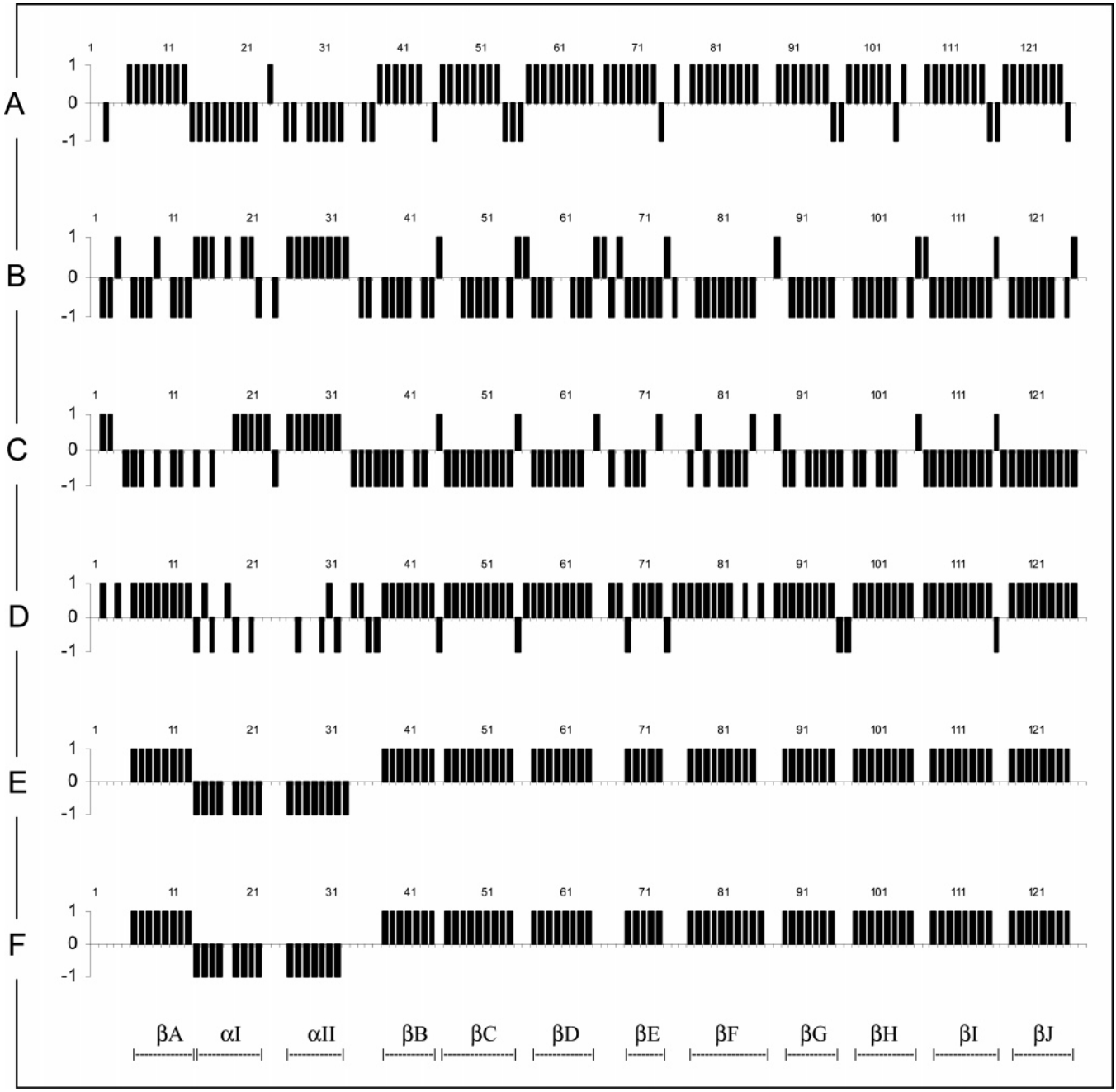

FIGURE 2: Holo-LFABP CSIs for H_α (A), C_α (B), CO (C), and C_β(D) resonances along with the resulting consensus CSI (E), plotted along the protein sequence. The consensus CSI determined for apo-LFABP (*44*) is shown for comparison in (F). Following standard practice (*49*), chemical shifts greater (or less) than the range determined for the random-coil form (0) of each amino acid in a database of 75 proteins are designated as +1 (or −1); contiguous groupings of +1 and −1 designations for the consensus CSI are assigned as β-strand and α-helix secondary structural elements, respectively.

and two α-helices spanning N14−M22 and E26−K33/*G32*, respectively.

Tertiary Structure Determination for Holo-LFABP with Two Oleates. The holo structures were generated using CNS/ARIA with geometric restraints derived from 2614 intramolecular NOEs, together with 34 hydrogen bonds, 62 values of vicinal coupling constants ($^3J_{H^N H^\alpha}$), and 185 dihedral angle restraints predicted from TALOS. No RDCs were included because substantial site-specific perturbations of the ^{15}N and ^{13}C HSQC spectra upon addition of $C_{12}E_5$ suggested release of some oleate from the protein and partitioning into the orienting medium. The topology parameters used for the calculation were modified by incorporating the oleate atom type as well as its geometry into the default CNS specifications. The highly consistent set of 10 lowest energy protein structures are displayed stereographically in Figure 3; the statistical data listed in Table 1 for holo-LFABP pertain to structures calculated for a protein sample containing two oleate ligands but without intermolecular NOEs to facilitate comparison with the apoprotein. (The protein−ligand complex is described below.) The excellent structural quality of the final holo structures is evidenced by the fact that 89% of the residues occupy the most favored region of Ramachandran space, the rare residues in disallowed regions involve only loops between secondary structural elements, and there are very few dihedral angle violations.

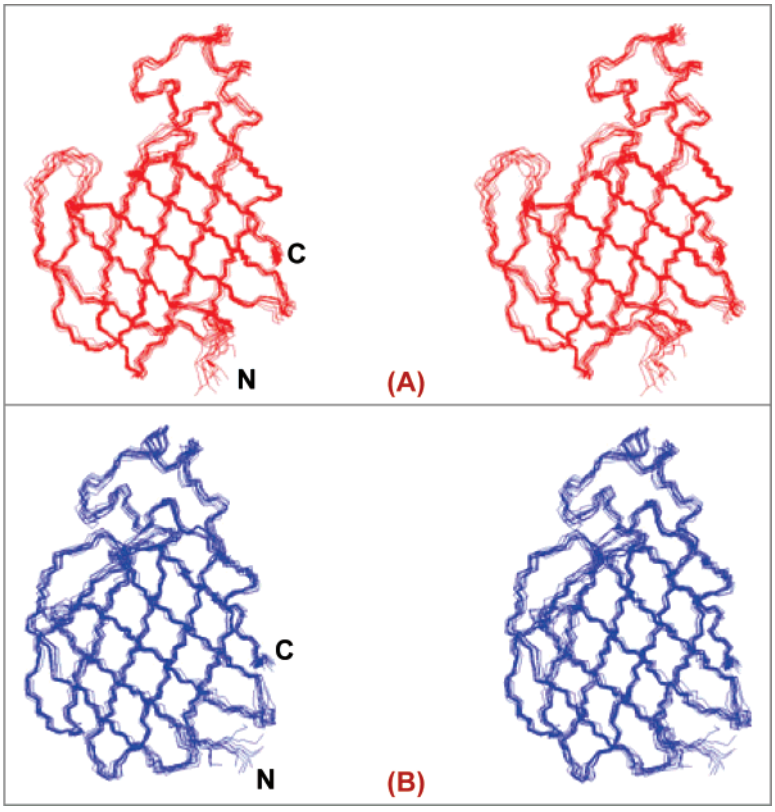

FIGURE 3: Comparison of NMR-derived conformations for apo-LFABP (A) and holo-LFABP (B), illustrated with MOLMOL stereodiagrams of the 10 lowest energy structures for each form of the protein. Designations for the secondary structural elements appear in Figure 4.

Table 1: Structural Statistics for 10 Final NMR Structures of Liver Fatty Acid-Binding Proteins[a]

	apo-LFABP	holo-LFABP[b]
NMR Constraints		
NOEs		
total intramolecular NOEs	2777	2614
intraresidue	1208	1223
sequential	492	570
medium-range (i < 4)	346	222
long-range	731	601
others		
hydrogen bonds	49	34
dihedral angles	182	185
^3J couplings	86	62
residual dipolar couplings	57	*c*
Structural Statistics		
average pairwise rms deviations (Å)		
backbone (secondary structure)	0.31 ± 0.049	0.43 ± 0.13
heavy atoms (secondary structure)	0.73 ± 0.054	0.85 ± 0.087
backbone (all residues)	0.48 ± 0.072	0.55 ± 0.16[d]
heavy atoms (all residues)	0.90 ± 0.094	0.99 ± 0.16
deviations from idealized geometry		
bond lengths (Å)	0.0054 ± 0.00012	0.0059 ± 0.00016
bond angles (deg)	0.607 ± 0.012	0.632 ± 0.017
impropers (deg)	0.593 ± 0.018	0.581 ± 0.027
Ramachandran plot (%)		
most favored	90.0	87.7
additionally allowed	8.37	8.82
generously allowed	1.26	1.71
disallowed	0.36	1.8

[a] The ARIA 2.0 program was used to determine 100 structures each for both apo- and holo-LFABP; results are shown for the 10 lowest energy structures. For calculation of the LFABP−ligand complex, 67 intermolecular NOEs were used with ARIA 1.2_dani. [b] Bound to two OLA ligands but determined without intermolecular NOEs. [c] One or both OLA ligands were expelled from the protein in aligning medium, as described in the text. [d] The rmsd for the oleate−LFABP complex determined with intermolecular NOEs was 0.77.

In terms of protein conformation, comparisons of the NMR structures with the previously published X-ray crystal structure of holo-LFABP (*1*) are made from the backbone traces and ribbon diagrams of Figure 4, which indicate excellent agreement between the solution and crystal states. Table 1 also lists the rmsd's calculated for this family of low-energy structures; this precision is compared below to both the apo-LFABP structure determined herein and IFABP data reported previously. The structural dependence of rmsd values for the family of superimposed solution structures shown in Figure 3 is examined in detail with the worm plot of Figure 5, which reveals the greatest holo-LFABP structural variability in the α-helices, along β-strands E and F, and in loops between the various β-strands.

Protein−Ligand Intermolecular Interactions. Whereas ^{13}C HSQC NMR has been used to demonstrate the presence of two chemically distinct bound oleates within the LFABP cavity (*46*), chemical shift perturbation analysis of apo- and holo-LFABP ^{15}N HSQC NMR spectra provides a preliminary indication of the corresponding protein sites that are modified structurally by ligand binding (*66*). Site-specific perturbations are found near the linker between helix II and strand B, near the turns between strands C and D and E and F, and at several locations within the cavity, though this analysis does not reveal which of the two ligands or which of their fatty acid molecular groupings is involved. An analysis of site-specific chemical shift perturbations and structural alterations during an oleate titration will be described elsewhere (Vela et al., to be submitted for publication).

A more precise comparison with the protein−ligand interactions revealed by X-ray crystallography in the hydrated solid state (*1*) can be made by direct determination of proximal spin pairs using intermolecular NOEs in solution-state NMR. In the case of the oleate−LFABP complex, this

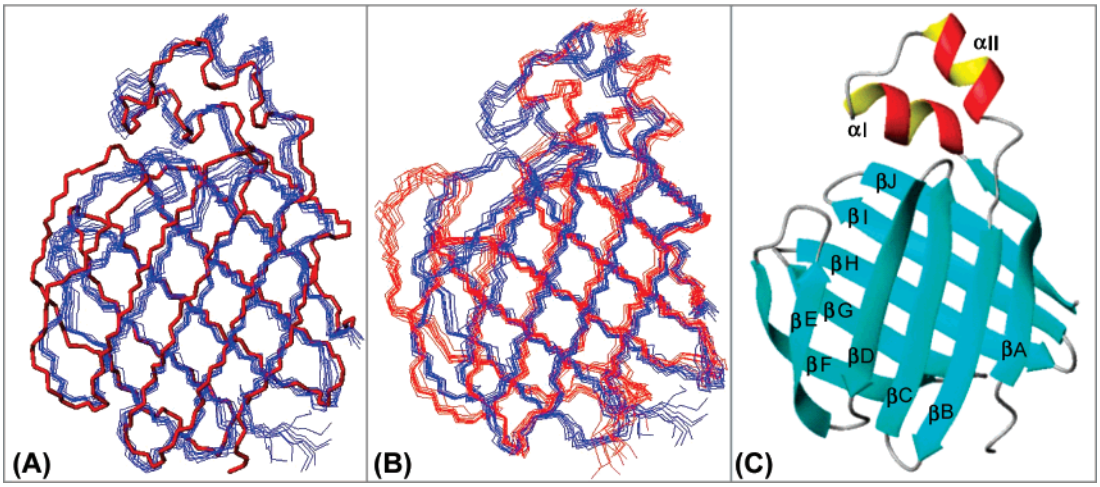

FIGURE 4: Comparison of solution and crystal structures for LFABPs using MOLMOL display: (A) superposition of a family of holo-LFABP solution structures (blue) with the crystal structure (thick red line); (B) superposition of lowest energy apo-LFABP (red) and holo-LFABP (blue) structures; (C) ribbon diagram of the lowest energy solution structure for apo-LFABP.

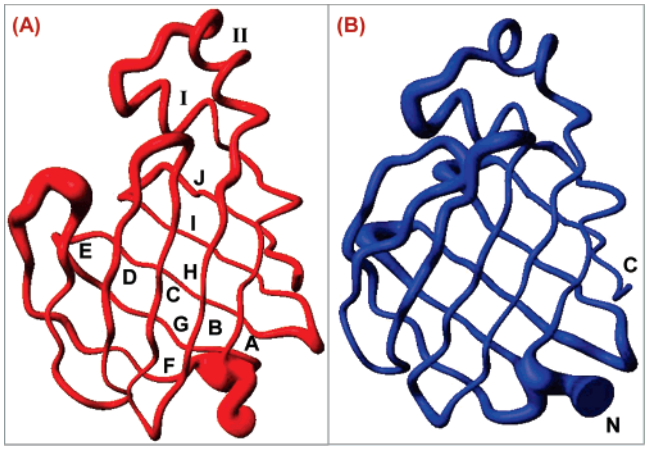

FIGURE 5: Variability in different regions of the NMR-derived LFABP structures. MOLMOL worm plots of the β-clam structures of apo-LFABP (red) and holo-LFABP (blue), using a trace thickness proportional to the square of the backbone rmsd of each helical, strand, or loop element of the protein. The bulge in strand G of the apoprotein corresponds to two distinct low-energy conformations found among the lowest energy structures (see Figures 3 and 4).

analysis is extremely challenging due to the presence of two identical ligands and the multiple chemical shift degeneracies of CH_2 groups and among the carboxylate group, double bond, and terminal methyl group of each oleate molecule. Nevertheless, it was possible to identify oleate ^1H and ^{13}C resonances corresponding to CH_3 groups and to those CH_2 groups adjacent to the carboxylate group and double bond. Determinations of which oleate was involved in a given NOESY connectivity were assisted by ^{15}N HSQC NMR results from a ligand titration series (Vela et al., personal communication), which indicate that the chemical shifts of residues I52, T93, and I109 are perturbed preferentially by the first entering ligand, whereas residues G32, I52, Y54, G55, S56, K57, M113, and Y120 are changed environmentally by entrance of the second ligand. Nonetheless, the CH_2 chemical shift degeneracies precluded assessment of the hydrophobic oleate−oleate interactions reported in the crystal structure (*1*). A total of 67 intermolecular NOEs were assigned in 3D NOE spectra of [U-^{15}N]LFABP/[U-^{13}C]oleate and [U-^{15}N/^{13}C]LFABP/oleate complexes and incorporated into the protein−ligand structure determination. As expected, the resulting backbone rmsd's exceed those in the holoprotein structure calculated without intermolecular NOEs (0.77 vs 0.55 for all backbone residues), but the respective complexes were very similar structurally (see below).

Through examination of the 50 lowest energy NMR solution structures of the oleate−LFABP complex, several populations of the extended oleate were identified: 14% displayed a conformation similar to the published X-ray structure, 50% adopted a second conformation, and the remaining 36% had variable conformations. Among the 25 lowest energy structures determined for the protein−ligand complex, the rmsd's for the major and minor conformations of the extended portal oleate were 1.4 and 1.7, respectively. For the U-shaped oleate molecule, 80% of the solution-state conformations resembled what was found in the crystal state and 20% had different conformations. For the internal oleate in its major conformation, the corresponding rmsd value was 1.45. Nonetheless, the protein conformations showed a high degree of consistency as noted above.

Parts A and B of Figure 6 show the conformation and location of the two oleate molecules within the protein cavity. Using a 4.0 Å distance cutoff between protons to assess protein−ligand interactions and considering the major NMR-derived conformation, the ligand with its carboxylate group close to the protein surface (OLA128, extended shape) was found to be proximal to residues L24, L28, K31, G32, I52, Y54, G55, S56, K57, I59, M74, M113, Y120, and R122 (Figure 6C), whereas the ligand deep within the cavity (OLA129, U shape) was close in space to residues I41, L50, I52, F63, L71, A81, V83, T93, F95, T102, F104, I109, N111, M113, and R122 (Figure 6D).

Tertiary Structure Determination for Apo-LFABP. As described for holo-LFABP, the structure calculation for apo-LFABP was conducted with CNS/ARIA as detailed in the Materials and Methods, initially using 2777 NOEs, 49 hydrogen bonds, 86 measurements of $^3J_{H^NH^\alpha}$ coupling, and 182 dihedral angle restraints predicted from TALOS. In agreement with chemical shift indices reported earlier (*44*), the tertiary structures included β-strands spanning G5−E13, S39−E44, K47−T51, N61−F63, E68−E72, K78−V82, K84−E86, M91−F95, I98−N105, T108−L115, and I118−R126 and helices spanning F15−M22 and E26−G32.

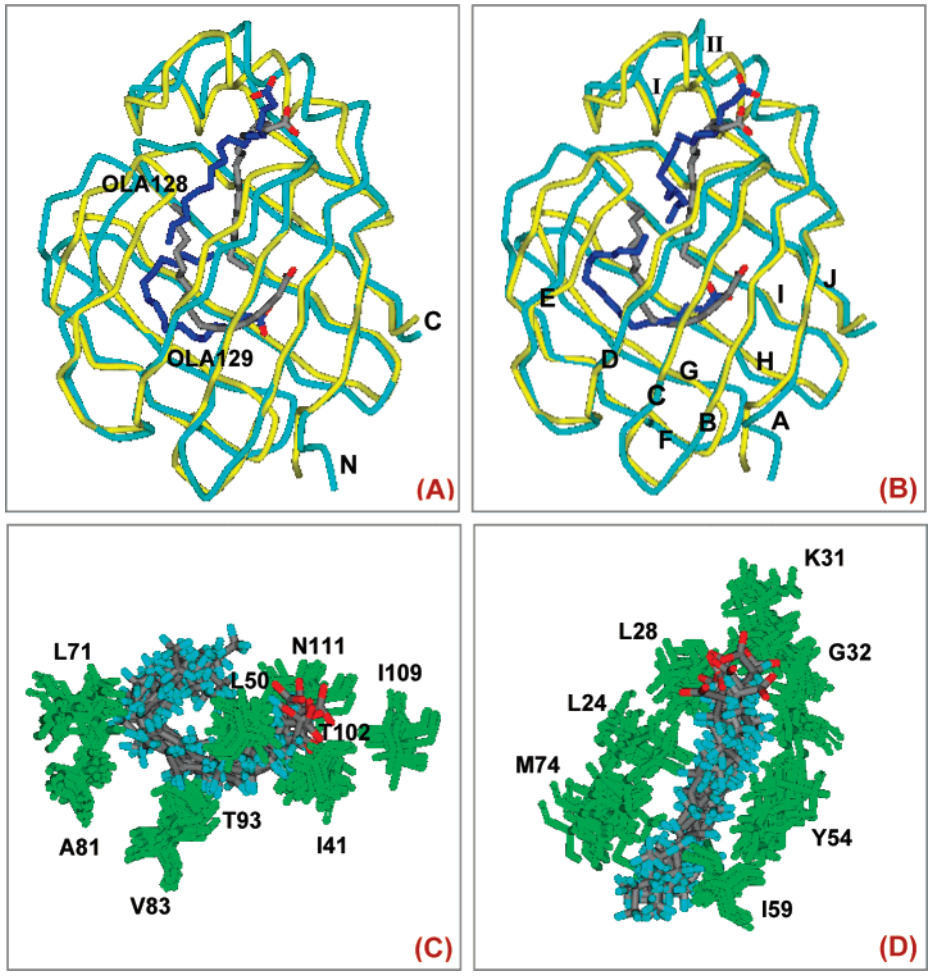

FIGURE 6: Conformations and locations of two oleate ligands complexed to LFABP, as deduced from calculations of the solution structure for the protein−ligand complex incorporating 67 intermolecular NOEs and displayed with DS ViewerPro. These results illustrate varied conformations of the extended OLA128 ligand as determined by NMR. (A) Overlaid Cα traces of the major conformation (50% of the structures, protein in cyan, ligand in blue) with X-ray results (*1*) (protein in yellow, ligand in gray). (B) Overlaid Cα traces of the minor NMR conformation (14% of the structures, protein in cyan, ligand in blue) with X-ray results (protein in yellow, ligand in gray). (C) Amino acid residues that interact with the U-shaped ligand (OLA129) in its major conformation. (D) Amino acid residues that interact with the extended-shaped ligand (OLA128) in its major conformation.

Although the β-barrel structural features of apo-LFABP were nearly superimposable with holo-LFABP (both the X-ray structure (*1*) and our NMR results (above)), the orientation of the apo-LFABP helices differed significantly from that of the holo-LFABP helices. To determine whether these were true structural differences or artifactual results stemming from a paucity of NOEs between protons in the helical and adjacent turn regions, additional experiments were conducted. In the presence of a $C_{12}E_5$ orienting medium, the ^{1}H chemical shifts of the protein were observed to change in a similar fashion and to a modest degree (mean of 0.04 ppm), permitting the measurement of 57 residual dipolar couplings (15 of them in the helical region) that refined the structure and confirmed the anomalous "open cap" orientation of the α-helices. The final ensemble of 10 lowest energy structures, for which inclusion of RDC data lowered the rmsd by ~0.3, is characterized statistically in Table 1 and presented as a stereodiagram in Figure 3. In addition to the consistency evidenced by the low rmsd value, the high quality of the NMR structure determination was verified using PROCHECK-NMR (*67*), which shows a small number of dihedral angle violations and a large percentage of residues (~90%) in the most favored region of Ramachandran space.

DISCUSSION

Resonance Assignments and Secondary Structural Elements. Figure 2 clearly shows the similarity in sequential location and length of secondary structural elements for the apo and holo forms of the LFABP protein, as detailed above. Figure 4B, which shows the ensembles of 10 lowest energy apo- and holo-LFABP structures from sets of 100 calculations, demonstrates that the β-strands and helices found within the polypeptide sequence are in good agreement with the predictions derived from chemical shift indices. Moreover, the secondary structural elements along the polypeptide chain of holo-LFABP in the solution state compare closely with those identified from the crystal structure (color-coded in Figure 1).

The residues in apo-LFABP for which backbone amide resonances are missing (in intermediate exchange) at pH 7.0 (G45, T53, S56, M74, G106, D107) are all located in the turns between β-strands, suggesting that these amino acids reside in solvent-exposed regions and/or experience a relatively high degree of conformational flexibility. Figure 4C confirms that these particular turns (B/C, C/D, E/F, H/I) are located at the top or bottom of the β-barrel, allowing for

both solvent exposure and structural fluctuations. Moreover, Figure 5 shows that these sites are among the most conformationally variable in the family of calculated NMR structures. Missing amide resonances and large rmsd's have also been reported for residues of apo-IFABP that exhibit discrete backbone disorder (*18*), for apo-CRABP(II) (*35*), and for apo-CRBP(II) (*19*). In contrast to the situation for apo-LFABP, the nearly complete set of amide backbone resonances observed for the holo form of the protein suggests that solvent exposure has been diminished and/or local structures have been stabilized as a consequence of ligand binding.

Tertiary Structure of Apo-LFABP in Solution. A worm plot in which the thickness corresponds to the square of the average backbone pairwise rmsd value (Figure 5A) confirms the well-defined β-barrel of apo-LFABP but reveals particular variability in the E/F loop, presumably because it is not "tethered" together with the helical portal region as in holo-LFABP. A plot of the number of geometric restraints vs polypeptide sequence (Supporting Information, Figure S2) shows an even distribution for both apo- and holoproteins, suggesting that the poorly defined regions are not attributable to a local paucity of NOEs or RDCs.

Among representative iLBP family members including apo-ILBP (PDB ID 1O1U (*29*)), apo-CRABP(II) (PDB ID 1BLR (*35*)), apo-CRBP(II) (PDB ID1B4M (*19*)), and apo-IFABP (PDB ID 1AEL (*18*)), the solution-state structures of all proteins exhibit a backbone-disordered region involving the loop following the second helix and turns between strands C and D, E and F, and G and H, as well as a wide gap between strands D and E. Other than these common features, the region between the C-terminus of the first helix and strand B differs structurally for apo-IFABP and apo-CRBP-(II) as compared with apo-LFABP and apo-CRABP(II): the former proteins have either a shorter helix II or no defined structure in that region, whereas the latter family members have more or less the same helix length as their corresponding holoproteins. Strikingly, the helix−turn−helix motif in apo-LFABP and apo-CRABP(II) is oriented in a fashion that opens the portal and leaves a much more aqueous-exposed protein cavity that could be more accessible to ligand entry.

A detailed comparison of the intestinal and liver protein sequences illustrates how subtle changes in the interactions among FABP residues may account for differences in the relative configurations of their respective β-barrel and α-helical structural elements. For instance, in apo-IFABP it is energetically favorable for helix II and its following loop to approach the βC/βD turn (*18*): hydrophobic interactions could occur between L30 and F55; moreover, hydrogen bond networks such as those found in the holoprotein (*18*) have the potential to link K29 to H33 and D34 to N54. The corresponding residues in LFABP are Q30, K31, D34, and I35 in helix II and the adjacent loop and G55 and S56 in the βC/βD turn (Figure 1). Interresidue hydrophobic interactions between the two LFABP regions are then disfavored: either Q30 or K31 of helix II might form hydrogen bonds with D34 of the loop or S56 of the βC/βD turn, though at most one hydrogen bond will be formed. The importance of hydrophobic interactions in bringing these regions into close proximity is also illustrated by other members of the FABP family: V33 with V58 in CRABP(II) and I33 with F58 in CRBP(II).

Tertiary Structure of Holo-LFABP in Solution and the Crystal State. Considering positions F3−I127 of the protein, the average pairwise rmsd's for these 10 structures are 0.55 and 0.99 Å for backbone and all heavy atoms, respectively (Table 1), about 50% better precision than for other holo-FABP NMR structures reported a decade ago (*68*−*70*) and 10−15% worse precision than for our apo-LFABP structures derived with additional RDC-based restraints. As for the apo form of the protein, the majority of residues have pairwise backbone rmsd values between 0.3 and 0.8 Å, consistent with a well-defined three-dimensional structure. Figure 4A shows that whereas the β-barrel is almost superimposable for holo-LFABP in solution and the crystal state, strands E and F deviate noticeably to yield an average backbone pairwise rmsd of 2.01 Å.

However, the presence of local structural heterogeneity is also evident: the worm plot (Figure 5B) makes it clear that the structure has both a well-defined β-barrel and several structurally variable elements—turns at the bottom of the cavity and a portal comprised of regions from the C-terminus of helix I to the loop following helix II and nearby turns between the β-strands (C/D, E/F, and G/H). The higher degree of consistency exhibited by the β-barrel supports its involvement in ligand binding but does not preclude ligand flexibility within a hydrogen-bonding network mediated by internal water molecules (*1*, *46*).

Tertiary Structure Comparison for Holo- and Apo-LFABP. As indicated above, both holo- and apo-LFABP structures are comprised of a β-barrel with a helix−turn−helix motif at one end (Figures 3 and 4). The β-barrel is well defined for both forms of the protein; the β-strand structural elements are also found to span similar sets of amino acid residues (noted above), and the β-sheets superimpose closely in most regions (Figure 4B). Both apo and holo forms of the protein exhibit reduced rmsd's if the helical regions at F15−M22 and E26−G32 and loops are excluded, evidencing particularly large conformational variability in the C/D and E/F strands; the holoprotein has additional conformational "hot spots" in the αI/αII turn (Figure 5).

The most striking structural difference between apo- and holo-LFABP involves the orientation of the helix−turn−helix "lid", which is no longer shut tightly over the entrance to the β-barrel in apo-LFABP and may expose the protein cavity to entering/exiting ligands or solvent molecules. In fact, Figure 4B reveals that, upon formation of the holoprotein, αI and the EF loop approach one another much more closely. Shortened distances for three hydrogen bonds between these regions are illustrated in Figure 7A−C. Analogous trends of open apo compared with closed holo states have been pointed out for apo-CRABP(II) in solution and holo-CRABP(II) as crystals (*34*), whereas in IFABP, ILBP, and CRBP(II) the holo- and apoprotein backbones both have helices that are "bent over" to cap the β-barrel. Thus, LFABP exhibits two related phenomena upon ligand binding: a closure of the lid of the β-barrel to stabilize the portal conformation (reported earlier for CRABP(II)) and a lessening of E/F conformational fluctuations (observed for ILBP, CRBP(II), and IFABP).

Ligand Binding and Solution-State Tertiary Structure of the Oleate−LFABP Complex. Despite the similar structural skeleton shared by all proteins of the iLBP family, the thermodynamic driving force for the binding of fatty acids

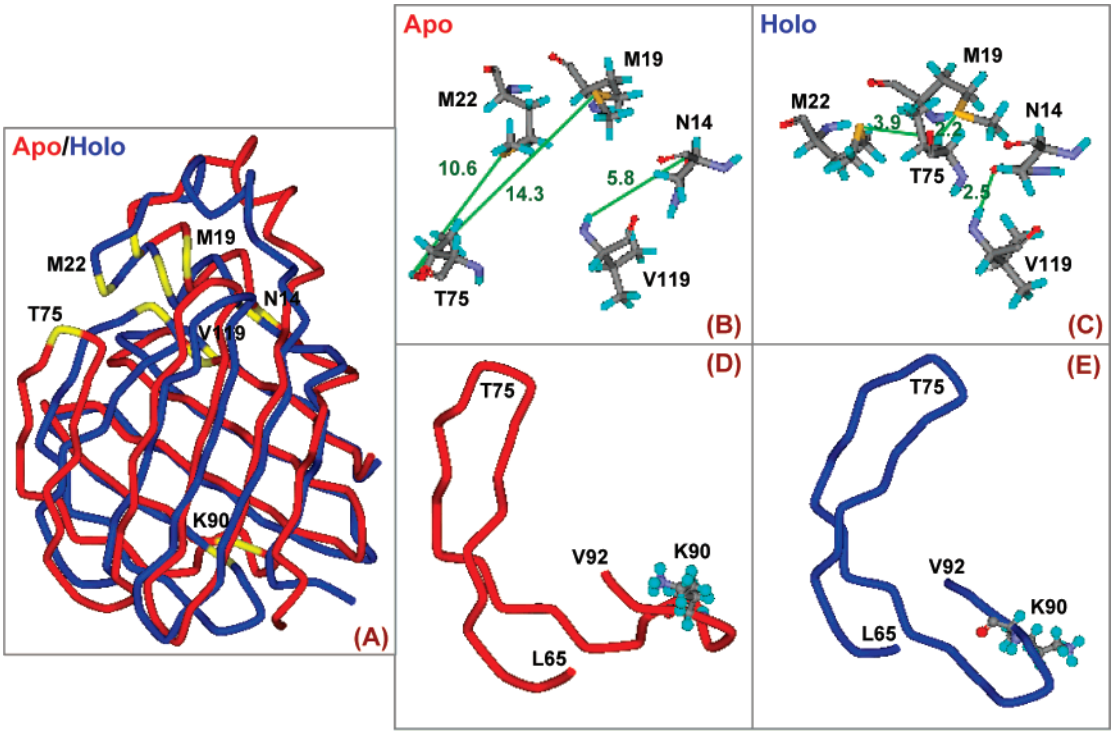

FIGURE 7: (A) Superposition of lowest energy apo-LFABP (red) and holo-LFABP (blue) ribbon structures with DS ViewerPro to illustrate altered geometries in the two forms. The approach of the EF loop to helix α1 is illustrated in panels B and C. The pivoting of K90 to "crack the whip" and pull the EF loop inward is shown by display of the L65−V92 fragment in panels D and E.

to LFABP includes significant entropic factors (~60% of ΔG for the first oleate ligand) associated with expulsion of ordered water (*71*) as well as the enthalpic contributions characteristic of IFABP and BFABP ligand binding (*20*, *72*). The change in enthalpy includes noncovalent terms involving electrostatic and hydrogen-bonding interactions between the fatty acid carboxylate group and positively charged residues (often arginine). The enthalpic component of oleate−LFABP interactions may also be understood using multiconformational continuum energy calculations (*73*): despite the energetically unfavorable desolvation of the carboxylate group expected upon ligand entry into the protein cavity, electrostatic interactions with a positive patch of the polypeptide structure (R122, K125, R126) provide the driving force for binding OLA129 (J. Mao and M. Gunner, personal communication). By contrast, the change in entropy upon water expulsion also permits hydrophobic interactions to occur—among residues of the polypeptide, between protein and ligand, and between ligands. The relatively large entropic contributions to binding affinity in LFABP suggest, then, that, as compared with IFABP and BFABP, hydrophobic effects play a more important role during the ligand-binding process. Given that LFABP uniquely accommodates two fatty acids within its cavity, it is plausible that these extra hydrophobic effects arise from interactions of the ligands with nonpolar protein residues and each other.

Although fatty acid-binding proteins such as BFABP, HFABP, MFABP, ILBP, IFABP, and LFABP each have at least two arginine residues in the cavity, they may exhibit contrasting interactions with the FA carboxylate group stemming from modest differences in protein sequence. The X-ray structures of these proteins reveal the following patterns of interaction: (i) for BFABP, HFABP, and MFABP, the COO^- group interacts with R126 and Y128 and indirectly with R106 through a water bridge; (ii) for IFABP, the COO^- group interacts with R106 but is not located proximally to R126 or F128; (iii) for LFABP, the COO^- group of the buried oleate (OLA129) is close in space to R122, S124, and S39.

Both the crystal structure (*1*) and our solution-state structure of the oleate−LFABP complex show two binding sites in the protein cavity (Figure 6). In solution one ligand is found to adopt a well-defined U shape that positions its long hydrophobic chain and ionized carboxylate deep within the cavity, whereas the other ligand has a more variable extended structure with its carboxylate group close to the surface. On the basis of intermolecular NOEs between the ligand and an overwhelmingly hydrophobic group of protein residues I41, L50, N61, L71, A81, V83, T93, T102, and I109 (Figure 6C), a close agreement with the crystal state results was found for 80% of the resulting conformations and the location of the interior oleate (OLA129). In those conformations the favorable entropic factors for the U-shaped ligand are achieved by interactions with the numerous hydrophobic amino acids lining the well-defined interior of the β-barrel, consistent with the ligand-binding thermodynamics cited above. For the portal oleate (OLA128), intermolecular NOEs were observed with protein residues L24, L28, G32, I35, I52, Y54, L57, I59, M74, Y120, and R122 (Figure 6D); additional proximities to OLA129 cannot be verified because of degeneracies in the NMR spectra of the ligands. The resulting structural refinement produced two major conformations (50% deviating from the crystal structure, Figure 6A; 14% in accord with the crystal structure, Figure 6B), in which the principal discrepancy concerns the orientation of the ligand tails. This ambiguity may reflect several factors: the lack of observable oleate−oleate interactions, uncertainty associated with facile chemical exchange between free and

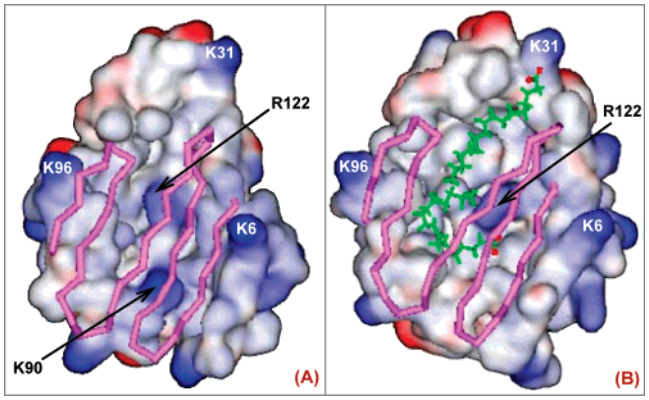

FIGURE 8: Electrostatic potential surface view at pH 7 of apo-LFABP (A) and the oleate−LFABP complex (B) displayed with DS ViewerPro. The calculation assumes that the Asp, Glu, Arg, and Lys residues are ionized, as predicted for 85% of the ionizable residues in a database of 490 proteins (*81*). The inner surfaces are displayed for residues 1−37 and 81−127, respectively. Surface charge diagrams show positive charges in blue, negative charges in red, and neutral charges in white; protein backbone traces (residues 38−80) and ligands are shown in pink and green, respectively. Note that K90 faces inward in (A) but swivels outward (Figure 7) and thus is not visible in (B).

bound ligands (*46*), and/or interaction of the extended ligand with a variety of portal residues that are themselves structurally disordered. Whereas the crystalline state appears to favor the conformation with the strongest hydrophobic oleate−oleate interactions, NMR measurements in solution yield low-energy structures with a significant range of ligand conformations, especially for the portal ligand.

To understand how the oleate molecules enter the LFABP cavity, it is instructive to examine electrostatic potential maps of the apo-LFABP structure. The electrostatic distribution for the cavity (Figure 8A) reveals two positively charged groups on the inner surface, K90 and R122. In contrast to previously reported structures of ILBP, CRABP(II), and IFABP (*18*, *29*, *35*), the K90 side chain of LFABP is located within the cavity rather than at the surface. Because K90 in apo-LFABP is located at the flexible turn between β-strands F and G (Figure 7D,E) and near the structurally variable strand G (Figure 5A), it should be able to swivel back and forth easily between the cavity and the outer surface. Thus, this additional positive charge located deep within the binding cavity may help to recruit the first fatty acid molecule (U-shaped OLA129). Then, once the carboxylate group establishes favorable interactions with R122, S124, and S39 through a hydrogen bond network including an ordered water molecule, the side chain of K90 could be pushed outward to generate a hydrophobic second binding site that accommodates the second ligand (the extended OLA128) without steric interference within the protein cavity. That swiveling action of K90 may also "crack the whip" to pull β-strand F and the E/F loop closer to helix I, as illustrated by comparing parts D and E of Figure 7. Furthermore, hydrophobic interactions of OLA128 with I59 (evidenced by an intermolecular NOE) could facilitate entry of the second oleate molecule. That ligand may bring the helix−turn−helix element closer to the β-barrel through both hydrophilic interactions of its carboxylate group with polar residue K31 and hydrophobic interactions of its fatty acyl chain with other nonpolar residues (L24, L28, and I35 shown in Figure 6D), ultimately covering the opening of the β-barrel. Evidence for favorable electrostatic interactions in the oleate−LFABP complex is summarized in Figure 8B, which shows a primarily hydrophobic cavity surface, the head-on orientation of the OLA129 carboxylate and the positively charged R122 (consistent with chemical shift changes in ^{13}C HSQC spectra) (*46*), and positioning of the OLA128 carboxylate near the protein surface. Analysis of ^{15}N HSQC data at several stages of an oleate titration is currently in progress to test these hypotheses (Vela et al., to be submitted for publication).

Finally, the present structural results offer a rationale for exit of oleate from LFABP. The internally bound ligand in IFABP is less exposed to solvent than the portal ligand in LFABP; the helix−turn−helix cap is closed in both apo and holo forms of the former protein. Release of oleate from IFABP may therefore require destabilization of the interaction between the second helix and the C/D turn, for instance by collision of the protein (via the second helix) with membranes, as we previously suggested (*42*, *74*). This hypothesis has recently gained support from a molecular dynamics simulation (*75*). However, for LFABP, both release and uptake of ligand by a diffusional mechanism (*14*, *15*) are favored by structures in which the orientation of the helix−turn−helix cap in LFABP is able to control exposure of the cavity to solvent. Previous analysis of a pair of I/LFABP chimeric proteins demonstrated that the transport mechanisms could be switched by exchanging the helical cap domains (*40*), further reinforcing the functional consequences of these divergent structural elements. Thus, exposure of the LFABP binding cavity to solvent may permit facile removal of OLA128 from the portal site, without the requirement of collisional activation. Moreover, a possible egress route through LFABP's unique gap between strands G and H has been suggested for the internally bound OLA129 (*1*, *46*). Conversely, uptake of the ligand by the apoprotein via a diffusional mechanism should be facilitated by the solvent-accessible open cap conformation. The structural differences found for IFABP and LFABP provide a plausible rationale for the two complementary modes of ligand binding and transfer, allowing for precise control of fatty acid metabolism and function within a single tissue type that could not be achieved by either protein alone.

Indeed, unique phenotypic characteristics of mice null for various FABPs strongly support the emerging concept of complementary as well as distinct functions for these different proteins. Recent studies using mice null for LFABP, for example, indicate a role in intestinal lipid secretion (*76*), the specific mechanism of which includes formation of prechylomicron transport vesicles within the enterocyte (*77*). In contrast, IFABP null mice exhibit systemic alterations in serum lipid profile (*78*); the fact that little or no compensatory change in intestinal FABP expression is observed in the LFABP null mouse, and vice versa (*78*−*80*), further indicates unique functions for these proteins, which are supported here by specific structural differences.

ACKNOWLEDGMENT

We are grateful to Drs. Alan Kleinfeld and Ron Ogata for the provision of rat LFABP cDNA. Gracious support from Drs. Lewis Kay, Ranjith Muhandiram, Frank Delaglio, Bruce Johnson, and Lei Zeng is also acknowledged for the

execution and interpretation of the NMR experiments. Drs. Marilyn Gunner and Junjun Mao conducted the MCCE calculations, and Ms. Adriana Vela assisted with the chemical shift perturbation analysis. Finally, we thank Drs. Andy Byrd and Art Palmer for valuable discussions and critical feedback during the course of this work.

SUPPORTING INFORMATION AVAILABLE

Chemical shifts (Table S1) and $^3J_{H^N H^\alpha}$ couplings (Table S2) for apo- and holo-LFABP, intermolecular NOE restraints between LFABP and oleates (Table S3, for holo-LFABP), residual dipolar couplings (Table S4) for apo-LFABP, hydrogen-bonded interactions (Table S5) for apo- and holo-LFABP, ^{15}N HSQC spectra of apo- and holo-LFABP with arginine side chain assignments (Figure S1), and histograms of NOE restraints (Figure S2). This material is available free of charge via the Internet at http://pubs.acs.org.

REFERENCES

1. Thompson, J., Winter, N., Terwey, D., Bratt, J., and Banaszak, L. (1997) The crystal structure of the liver fatty acid-binding protein. A complex with two bound oleates, *J. Biol. Chem. 272*, 7140−7150.
2. Glatz, J. F., and van der Vusse, G. J. (1996) Cellular fatty acid-binding proteins: their function and physiological significance, *Prog. Lipid Res. 35*, 243−282.
3. Coe, N. R., and Bernlohr, D. A. (1998) Physiological properties and functions of intracellular fatty acid-binding proteins, *Biochim. Biophys. Acta 1391*, 287−306.
4. Storch, J., and Thumser, A. E. (2000) The fatty acid transport function of fatty acid-binding proteins, *Biochim. Biophys. Acta 1486*, 28−44.
5. Glatz, J. F., Luiken, J. J., van Bilsen, M., and van der Vusse, G. J. (2002) Cellular lipid binding proteins as facilitators and regulators of lipid metabolism, *Mol. Cell Biochem. 239*, 3−7.
6. Zimmerman, A. W., and Veerkamp, J. H. (2002) New insights into the structure and function of fatty acid-binding proteins, *Cell. Mol. Life Sci. 59*, 1096−1116.
7. Hamilton, J. (2004) Fatty acid interactions with proteins: what X-ray crystal and NMR solution structures tell us, *Prog. Lipid Res.* 1−23.
8. Weisiger, R. A. (2002) Cytosolic fatty acid binding proteins catalyze two distinct steps in intracellular transport of their ligands, *Mol. Cell Biochem. 239*, 35−43.
9. Richieri, G. V., Ogata, R. T., and Kleinfeld, A. M. (1996) Thermodynamic and kinetic properties of fatty acid interactions with rat liver fatty acid-binding protein, *J. Biol. Chem. 271*, 31068−31074.
10. Thompson, J., Reese-Wagoner, A., and Banaszak, L. (1999) Liver fatty acid binding protein: species variation and the accommodation of different ligands, *Biochim. Biophys. Acta 1441*, 117−130.
11. Thompson, J., Ory, J., Reese-Wagoner, A., and Banaszak, L. (1999) The liver fatty acid binding protein−comparison of cavity properties of intracellular lipid-binding proteins, *Mol. Cell Biochem. 192*, 9−16.
12. Wang, H., He, Y., Hsu, K. T., Magliocca, J. F., Storch, J., and Stark, R. E. (1998) ^{1}H, ^{15}N and ^{13}C resonance assignments and secondary structure of apo liver fatty acid-binding protein, *J. Biomol. NMR 12*, 197−199.
13. Thumser, A. E. A., and Wilton, D. C. (1996) The binding of cholesterol and bile salts to recombinant rat liver fatty acid-binding protein, *Biochem. J. 320*, 729−733.
14. Hsu, K. T., and Storch, J. (1996) Fatty acid transfer from liver and intestinal fatty acid-binding proteins to membranes occurs by different mechanisms, *J. Biol. Chem. 271*, 13317−13323.
15. Thumser, A. E., and Storch, J. (2000) Liver and intestinal fatty acid-binding proteins obtain fatty acids from phospholipid membranes by different mechanisms, *J. Lipid Res. 41*, 647−656.
16. Thumser, A. E., Tsai, J., and Storch, J. (2001) Collision-mediated transfer of long-chain fatty acids by neural tissue fatty acid-binding proteins (FABP): studies with fluorescent analogs, *J. Mol. Neurosci. 16*, 143−150.
17. Hodsdon, M. E., and Cistola, D. P. (1997) Ligand binding alters the backbone mobility of intestinal fatty acid-binding protein as monitored by ^{15}N NMR relaxation and ^{1}H exchange, *Biochemistry 36*, 2278−2290.
18. Hodsdon, M. E., and Cistola, D. P. (1997) Discrete backbone disorder in the nuclear magnetic resonance structure of apo intestinal fatty acid-binding protein: implications for the mechanism of ligand entry, *Biochemistry 36*, 1450−1460.
19. Lu, J., Lin, C. L., Tang, C., Ponder, J. W., Kao, J. L., Cistola, D. P., and Li, E. (1999) The structure and dynamics of rat apo-cellular retinol-binding protein II in solution: comparison with the X-ray structure, *J. Mol. Biol. 286*, 1179−1195.
20. Balendiran, G. K., Schnutgen, F., Scapin, G., Borchers, T., Xhong, N., Lim, K., Godbout, R., Spener, F., and Sacchettini, J. C. (2000) Crystal structure and thermodynamic analysis of human brain fatty acid-binding protein, *J. Biol. Chem. 275*, 27045−27054.
21. Lu, J., Lin, C.-L., Tang, C., Ponder, J. W., Kao, J. L. F., Cistola, D. P., and Li, E. (2000) Binding of retinol induces changes in rat cellular retinol-binding protein II conformation and backbone dynamics, *J. Mol. Biol. 300*, 619−632.
22. Jakobsson, E., Alvite, G., Bergfors, T., Esteves, A., and Kleywegt, G. J. (2003) The crystal structure of Echinococcus granulosus fatty-acid-binding protein 1, *Biochim. Biophys. Acta 1649*, 40−50.
23. Hohoff, C., Borchers, T., Rustow, B., Spener, F., and van Tilbeurgh, H. (1999) Expression, purification, and crystal structure determination of recombinant human epidermal-type fatty acid binding protein, *Biochemistry 38*, 12229−12239.
24. Reese-Wagoner, A., Thompson, J., and Banaszak, L. (1999) Structural properties of the adipocyte lipid binding protein, *Biochim. Biophys. Acta 1441*, 106−116.
25. Lucke, C., Rademacher, M., Zimmerman, A. W., Van Moerkerk, H. T., Veerkamp, J. H., and Ruterjans, H. (2001) Spin-system heterogeneities indicate a selected-fit mechanism in fatty acid binding to heart-type fatty acid-binding protein (H-FABP), *Biochem. J. 354*, 259−266.
26. Franzoni, L., Lucke, C., Perez, C., Cavazzini, D., Rademacher, M., Ludwig, C., Spisni, A., Rossi, G. L., and Ruterjans, H. (2002) Structure and backbone dynamics of Apo- and holo-cellular retinol-binding protein in solution, *J. Biol. Chem. 277*, 21983−21997.
27. Gutierrez-Gonzalez, L. H., Ludwig, C., Hohoff, C., Rademacher, M., Hanhoff, T., Ruterjans, H., Spener, F., and Lucke, C. (2002) Solution structure and backbone dynamics of human epidermal-type fatty acid-binding protein (E-FABP), *Biochem. J. 364*, 725−737.
28. Rademacher, M., Zimmerman, A. W., Ruterjans, H., Veerkamp, J. H., and Lucke, C. (2002) Solution structure of fatty acid-binding protein from human brain, *Mol. Cell Biochem. 239*, 61−68.
29. Kurz, M., Brachvogel, V., Matter, H., Stengelin, S., Thuring, H., and Kramer, W. (2003) Insights into the bile acid transportation system: the human ileal lipid-binding protein-cholyltaurine complex and its comparison with homologous structures, *Proteins 50*, 312−328.
30. Di Pietro, S. M., Corsico, B., Perduca, M., Monaco, H. L., and Santome, J. A. (2003) Structural and biochemical characterization of toad liver fatty acid-binding protein, *Biochemistry 42*, 8192−8203.
31. Vasile, F., Ragona, L., Catalano, M., Zetta, L., Perduca, M., Monaco, H., and Molinari, H. (2003) Solution structure of chicken liver basic fatty acid binding protein, *J. Biomol. NMR 25*, 157−160.
32. Constantine, K. L., Friedrichs, M. S., Wittekind, M., Jamil, H., Chu, C. H., Parker, R. A., Goldfarb, V., Mueller, L., and Farmer, B. T. (1998) Backbone and side chain dynamics of uncomplexed human adipocyte and muscle fatty acid-binding proteins, *Biochemistry 37*, 7965−7980.
33. Lu, J., Lin, C. L., Tang, C., Ponder, J. W., Kao, J. L., Cistola, D. P., and Li, E. (2000) Binding of retinol induces changes in rat cellular retinol-binding protein II conformation and backbone dynamics, *J. Mol. Biol. 300*, 619−632.
34. Thompson, J. R., Bratt, J. M., and Banaszak, L. J. (1995) Crystal structure of cellular retinoic acid binding protein I shows increased access to the binding cavity due to formation of an intermolecular beta-sheet, *J. Mol. Biol. 252*, 433−446.
35. Wang, L., Li, Y., Abildgaard, F., Markley, J. L., and Yan, H. (1998) NMR solution structure of type II human cellular retinoic acid binding protein: implications for ligand binding, *Biochemistry 37*, 12727−12736.

36. Chen, X., Tordova, M., Gilliland, G. L., Wang, L., Li, Y., Yan, H., and Ji, X. (1998) Crystal structure of apo-cellular retinoic acid-binding protein type II (R111M) suggests a mechanism of ligand entry, *J. Mol. Biol. 278*, 641−653.
37. Honma, Y., Niimi, M., Uchiumi, T., Takahashi, Y., and Odani, S. (1994) Evidence for conformational change of fatty acid-binding protein accompanying binding of hydrophobic ligands, *J. Biochem. (Tokyo) 116*, 1025−1029.
38. Jamison, R. S., Newcomer, M. E., and Ong, D. E. (1994) Cellular retinoid-binding proteins: limited proteolysis reveals a conformational change upon ligand binding, *Biochemistry 33*, 2873−2879.
39. Lucke, C., Fushman, D., Ludwig, C., Hamilton, J., Sacchettini, J. C., and Ruterjans, H. (1999) A comparative study of the backbone dynamics of two closely related lipid binding proteins: Bovine heart fatty acid binding protein and porcine ileal lipid binding protein, *Mol. Cell Biochem. 192*, 109−121.
40. Corsico, B., Liou, H. L., and Storch, J. (2004) The alpha-helical domain of liver fatty acid binding protein is responsible for the diffusion-mediated transfer of fatty acids to phospholipid membranes, *Biochemistry 43*, 3600−3607.
41. Steele, R. A., Emmert, D. A., Kao, J., Hodsdon, M. E., Frieden, C., and Cistola, D. P. (1998) The three-dimensional structure of a helix-less variant of intestinal fatty acid-binding protein, *Protein Sci. 7*, 1332−1339.
42. Corsico, B., Cistola, D. P., Frieden, C., and Storch, J. (1998) The helical domain of intestinal fatty acid binding protein is critical for collisional transfer of fatty acids to phospholipid membranes, *Proc. Natl. Acad. Sci. U.S.A. 95*, 12174−12178.
43. Wu, F., Corsico, B., Flach, C. R., Cistola, D. P., Storch, J., and Mendelsohn, R. (2001) Deletion of the helical motif in the intestinal fatty acid-binding protein reduces its interactions with membrane monolayers: Brewster angle microscopy, IR reflection-absorption spectroscopy, and surface pressure studies, *Biochemistry 40*, 1976−1983.
44. Wang, H., He, Y., Hsu, K. T., Magliocca, J. F., Storch, J., and Stark, R. E. (1998) ^{1}H, ^{15}N and ^{13}C resonance assignments and secondary structure of apo liver fatty acid-binding protein, *J. Biomol. NMR 12*, 197−199.
45. Yang, X., Wang, H., He, Y., Francis, F., Kodukula, S., Storch, J., and Stark, R. E. (2004) Structural divergence in the lipid portal region of rat liver fatty acid-binding protein upon binding of long-chain fatty acids, Experimental NMR Conference, Abstract.
46. Wang, H., He, Y., Kroenke, C. D., Kodukula, S., Storch, J., Palmer, A. G., and Stark, R. E. (2002) Titration and exchange studies of liver fatty acid-binding protein with ^{13}C-labeled long-chain fatty acids, *Biochemistry 41*, 5453−5461.
47. Marley, J., Lu, M., and Bracken, C. (2001) A method for efficient isotopic labeling of recombinant proteins, *J. Biomol. NMR 20*, 71−75.
48. Ruckert, M., and Otting, G. (2000) Alignment of Biological Macromolecules in Novel Nonionic Liquid Crystalline Media for NMR Experiments, *J. Am. Chem. Soc. 122*, 7793−7797.
49. Wishart, D. S., and Sykes, B. D. (1994) The ^{13}C chemical-shift index: a simple method for the identification of protein secondary structure using ^{13}C chemical-shift data, *J. Biomol. NMR 4*, 171−180.
50. Cavanagh, J., Fairbrother, W. J., Palmer, A. G., III, Rance, M., and Skelton, N. J. (2006) *Protein NMR Spectroscopy: Principles and Practice*, Elsevier Academic Press, Burlington, MA.
51. Yamazaki, T., Forman-Kay, J. D., and Kay, L. E. (1993) Two-dimensional NMR experiments for correlating carbon-13.beta. and proton.delta./.epsilon. chemical shifts of aromatic residues in ^{13}C-labeled proteins via scalar couplings, *J. Am. Chem. Soc. 115*, 11054−11055.
52. Prompers, J. J., Groenewegen, A., Hilbers, C. W., and Pepermans, H. A. M. (1998) Two-dimensional NMR experiments for the assignment of aromatic side chains in ^{13}C-labeled proteins, *J. Magn. Reson. 130*, 68−75.
53. Wang, Y.-X., Jacob, J., Wingfield, P. T., Palmer, I., Stahl, S. J., Kaufman, J. D., Huang, P. L., Lee-Haung, S., and Torchia, D. A. (2000) Anti-HIV and anti-tumor protein MAP30, a 30 kDa single-strand type-I RIP, shares similar secondary structure and β-sheet topology with the A chain of ricin, a type-II RIP, *Protein Sci. 9*, 138−144.
54. Sudmeier, J. L., Ash, E. L., Gunther, U. L., Luo, X., Bullock, P. A., and Bachovchin, W. W. (1996) HCN, a triple-resonance NMR technique for selective observation of histidine and tryptophan side chains in ^{13}C/^{15}N-labeled proteins, *J. Magn. Reson. 113B*, 236−247.
55. Delaglio, F., Grzesiek, S., Vuister, G. W., Zhu, G., Pfeifer, J., and Bax, A. (1995) NMRPipe: a multidimensional spectral processing system based on UNIX pipes, *J. Biomol. NMR 6*, 277−293.
56. Johnson, B. A., and Blevins, R. A. (1994) NMR View: A computer program for the visualization and analysis of NMR data, *J. Biomol. NMR 4*, 603−614.
57. Zhang, O., Kay, L. E., Olivier, J. P., and Forman-Kay, J. D. (1994) Backbone ^{1}H and ^{15}N resonance assignments of the N-terminal SH3 domain of drk in folded and unfolded states using enhanced-sensitivity pulsed field gradient NMR techniques, *J. Biomol. NMR 4*, 845−858.
58. Zwahlen, C., Legault, P., Vincent, S. J. F., Greenblatt, J., Konrat, R., and Kay, L. E. (1997) Methods for measurement of intermolecular NOEs by multinuclear NMR spectroscopy: Application to a bacteriophage lambda N-peptide/boxB RNA complex, *J. Am. Chem. Soc. 119*, 6711−6721.
59. Kuboniwa, H., Grzesiek, S., Delaglio, F., and Bax, A. (1994) Measurement of HN-Hα J couplings in calcium-free calmodulin using new 2D and 3D water-flip-back methods, *J. Biomol. NMR 4*, 871−878.
60. Cornilescu, G., Delaglio, F., and Bax, A. (1999) Protein backbone angle restraints from searching a database for chemical shift and sequence homology, *J. Biomol. NMR 13*, 289−302.
61. Ottiger, M., Delaglio, F., and Bax, A. (1998) Measurement of J and dipolar couplings from simplified two-dimensional NMR spectra, *J. Magn. Reson. 131*, 373−378.
62. Brunger, A. T., Adams, P. D., Clore, G. M., DeLano, W. L., Gros, P., Jiang, J. S., Kuszewski, J., Nilges, M., Pannu, N. S., Read, R. J., Rice, L. M., Simonson, T., and Warren, G. L. (1998) Crystallography & NMR system: A new software suite for macromolecular structure determination, *Acta Crystallogr., D: Biol. Crystallogr. 54*, 905−921.
63. Linge, J. P., O'Donoghue, S. I., and Nilges, M. (2001) Automated assignment of ambiguous nuclear Overhauser effects with ARIA, *Methods Enzymol. 339*, 71−90.
64. Linge, J. P., Williams, M. A., Spronk, C. A. E. M., Bonvin, A. M. J. J., and Nilges, M. (2003) Refinement of protein structures in explicit solvent, *Proteins: Struct., Funct., Genet. 50*, 496−506.
65. Wishart, D. S., and Sykes, B. D. (1994) Chemical shifts as a tool for structure determination, *Methods Enzymol. 239*, 363−392.
66. Shuker, S. B., Hajduk, P. J., Meadows, R. P., and Fesik, S. W. (1996) Discovering high-affinity ligands for proteins: SAR by NMR, *Science 274*, 1531−1534.
67. Laskowski, R. A., Rullmannn, J. A., MacArthur, M. W., Kaptein, R., and Thornton, J. M. (1996) AQUA and PROCHECK-NMR: programs for checking the quality of protein structures solved by NMR, *J. Biomol. NMR 8*, 477−486.
68. Hodsdon, M. E., Ponder, J. W., and Cistola, D. P. (1996) The NMR solution structure of intestinal fatty acid-binding protein complexed with palmitate: application of a novel distance geometry algorithm, *J. Mol. Biol. 264*, 585−602.
69. Zhang, F., Lucke, C., Baier, L. J., Sacchettini, J. C., and Hamilton, J. A. (1997) Solution structure of human intestinal fatty acid binding protein: implications for ligand entry and exit, *J. Biomol. NMR 9*, 213−228.
70. Lassen, D., Lucke, C., Kveder, M., Mesgarzadeh, A., Schmidt, J. M., Specht, B., Lezius, A., Spener, F., and Ruterjans, H. (1995) Three-dimensional structure of bovine heart fatty-acid-binding protein with bound palmitic acid, determined by multidimensional NMR spectroscopy, *Eur. J. Biochem. 230*, 266−280.
71. Rolf, B., Oudenampsen-Kruger, E., Borchers, T., Faergeman, N. J., Knudsen, J., Lezius, A., and Spener, F. (1995) Analysis of the ligand binding properties of recombinant bovine liver-type fatty acid binding protein, *Biochim. Biophys. Acta 1259*, 245−253.
72. Miller, K. R., and Cistola, D. P. (1993) Titration calorimetry as a binding assay for lipid-binding proteins, *Mol. Cell Biochem. 123*, 29−37.
73. Alexov, E. G., and Gunner, M. (1997) Incorporating protein conformational flexibility into the calculation of pH-dependent protein properties, *Biophys. J. 72*, 2075−2093.
74. Falomir-Lockhart, L. J., Kahn, P. C., Storch, J., and Corsico, B. (2006) Protein-membrane interaction and fatty acid transfer from intestinal fatty acid binding protein to membranes: Support for a multistep process, *J. Biol. Chem. 281*, 14232−14240.

75. Mihajlovic, M., and Lazaridis, T. (2007) Modeling fatty acid delivery from intestinal fatty acid binding protein to a membrane, *Protein Sci. 16*, 2042−2055.
76. Newberry, E. P., Xie, Y., Kennedy, S. M., Luo, J., and Davidson, N. O. (2006) Protection against Western diet-induced obesity and hepatic steatosis in liver fatty acid-binding protein knockout mice, *Hepatology 44*, 1191−1205.
77. Neeli, I., Siddiqi, S. A., Siddiqi, S., Lagakos, W. S., Binas, B., Gheyi, T., Storch, J., and Mansbach, C. M. II (2007) Liver fatty acid-binding protein initiates budding of pre-chylomicron transport vesicles from intestinal endoplasmic reticulum, *J. Biol. Chem. 282*, 17974−17984.
78. Vassileva, G., Huwyler, L., Poirier, K., Agellon, L. B., and Toth, M. J. (2000) The intestinal fatty acid binding protein is not essential for dietary fat absorption in mice, *FASEB J. 14*, 2040−2046.
79. Lagakos, W. S., Zhou, Y. X., and Storch, J. (2007) Intestinal lipid metabolism is altered in liver FABP knockout mice, *FASEB J. 21*, 231.6
80. Newberry, E. P., Xie, Y., Kennedy, S., Han, X., Buhman, K. K., Luo, J., Gross, R. W., and Davidson, N. O. (2003) Decreased hepatic triglyceride accumulation and altered fatty acid uptake in mice with deletion of the liver fatty acid-binding protein gene, *J. Biol. Chem. 278*, 51664−51672.
81. Kim, J., Mao, J., and Gunner, M. R. (2005) Are acidic and basic groups in buried proteins predicted to be ionized? *J. Mol. Biol. 348*, 1283−1298.

BI701092R